

Journal of Materials Chemistry A

Accepted Manuscript



This is an *Accepted Manuscript*, which has been through the Royal Society of Chemistry peer review process and has been accepted for publication.

Accepted Manuscripts are published online shortly after acceptance, before technical editing, formatting and proof reading. Using this free service, authors can make their results available to the community, in citable form, before we publish the edited article. We will replace this *Accepted Manuscript* with the edited and formatted *Advance Article* as soon as it is available.

You can find more information about *Accepted Manuscripts* in the [Information for Authors](#).

Please note that technical editing may introduce minor changes to the text and/or graphics, which may alter content. The journal's standard [Terms & Conditions](#) and the [Ethical guidelines](#) still apply. In no event shall the Royal Society of Chemistry be held responsible for any errors or omissions in this *Accepted Manuscript* or any consequences arising from the use of any information it contains.

Improved Electrochemical Performance and Capacity Fading Mechanism of Nano-sized $\text{LiMn}_{0.9}\text{Fe}_{0.1}\text{PO}_4$ Cathode Modified by Polyacene Coating

Cite this: DOI: 10.1039/x0xx00000x

Received 00th January 2014,
Accepted 00th January 2014

DOI: 10.1039/x0xx00000x

www.rsc.org/

Liguang Wang^a, Pengjian Zuo^{*a}, Geping Yin^a, Yulin Ma^a, Xinqun Cheng^a,
Chunyu Du^a, Yunzhi Gao^a

Nano-sized $\text{LiMn}_{1-x}\text{Fe}_x\text{PO}_4$ ($x = 0$ and 0.1) was prepared by a solvothermal method in a mixed solvent of water and ethanol. $\text{LiMn}_{0.9}\text{Fe}_{0.1}\text{PO}_4$ -polyacene (PAS) composite exhibits a high conductivity ($0.15 \text{ S}\cdot\text{cm}^{-1}$) resulting in an excellent rate performance and good cycle life. The $\text{LiMn}_{0.9}\text{Fe}_{0.1}\text{PO}_4$ -PAS composite delivers a discharge capacity of 161, 141, and 107 $\text{mAh}\cdot\text{g}^{-1}$ at 0.1 C, 1 C and 10 C, respectively. The well-distributed conductive polyacene surrounding the $\text{LiMn}_{0.9}\text{Fe}_{0.1}\text{PO}_4$ nanoplates enhances the electronic contact of the nanosized crystalline particles and suppresses the manganese dissolution related to the structure evolution during cycling. Specifically, the manganese dissolution, electrolyte decomposition and the antisite defects are the significant factors that impact the capacity degradation of olivine iron-doped lithium manganese phosphate cathode materials.

Introduction

Rapid consumption of fossil fuels and raising environmental concerns bring great scientific and technological challenges for developing the sustainable energy storage and conversion systems. During the past decades, lithium ion batteries (LIBs), due to their high energy density, safety and good cycleability, have been dominating the market of power sources for electronic devices, such as laptop and smart phones, and extending the application in electric vehicles (EVs), hybrid electric vehicles (HEVs) and energy storage systems.^{1,2} Herein, the orthorhombic structured phosphor-olivine LiMPO_4 ($M = \text{Fe}$, Mn , Co and Ni) materials have been intensively investigated as an attractive positive electrode material for high-performance lithium ion batteries owing to their high capacity, thermal stability, environmental benignity and low cost since the first literature on lithium transition metal phosphates was reported by Padhi et al. in 1997.^{3,4} The strong covalent P-O bonds in the tetrahedral $(\text{PO}_4)^{3-}$ anion restrain oxygen loss and improve the structure stability of LiMnPO_4 .⁵ Among olivine cathodes, LiMnPO_4 is a good alternative to LiFePO_4 with similar specific capacity (170 mA h g^{-1}) but higher operating voltage (4.1 V vs. Li^+/Li) from the $\text{Mn}^{2+}/\text{Mn}^{3+}$ redox couple.³ However, LiMnPO_4 suffers from the low electronic conductivity ($< 10^{-10} \text{ S}\cdot\text{cm}^{-1}$, compared with $1.8 \times 10^{-8} \text{ S}\cdot\text{cm}^{-1}$ for LiFePO_4),⁶ high surface energy barrier for Li diffusion,^{7,8} a large kinetic barrier to ion and electron hopping at the phase boundary resulting from the Jahn-Teller distortion^{6,9-11} and meta-stability of the delithiated phase.^{12,13} To date, a comprehensive understanding of the structure evolution and capacity fading mechanism has not yet been established, and fortunately the improved electrochemical performance of lithium manganese phosphate cathode materials has been reported extensively. Previous results on enhancing the electrochemical performance of LiMnPO_4 mainly focused on (i) particle size minimizing, which reduces the diffusion length for lithium ion transport and also offers high surface area leading to the enhanced rate capability and power density,¹³⁻¹⁶ (ii) surface coating with electronically conductive material, which improves the electronic conductivity and allows electrons to tunnel through the active materials. Herein, most researchers adopted abundant carbon of over 10 wt% to

enhance the electrochemical performance of LiMnPO_4 .¹⁷⁻²¹ (iii) guest ion doping such as Fe^{2+} , Mg^{2+} , V^{3+} and Co^{2+} .²²⁻²⁷ For the cation doping that have been explored, the iron-substituted LiMnPO_4 materials denoted as $\text{LiMn}_{1-x}\text{Fe}_x\text{PO}_4$ with large range of substitution (x from 0 to 1) have thus far provided the best electrochemical performance.²⁸

In order to compensate the intrinsic low electronic conductivity of LiMnPO_4 , the conductive carbon coating is the straightforward method for limiting the crystalline growing size and enhancing the electronic contact among the nanocrystals to subsequently achieve the good rate performance and cycleability. S. M. Oh et al synthesized the LiMnPO_4 material containing 30 wt% carbon by ultrasonic spray pyrolysis followed by ball milling, and this material achieved a discharge capacity of 158 $\text{mAh}\cdot\text{g}^{-1}$ at the rate of C/20.¹⁷ LiMnPO_4/C cathode materials were synthesized by a supercritical ethanol process, and the resulting material showed good capacity and delivered a practical capacity of 156 $\text{mAh}\cdot\text{g}^{-1}$ at 0.01 C.²⁹ More recently, X. Rui et al developed a liquid-phase exfoliation approach combined with a solvothermal lithiation process for the fabrication of ultrathin LiMnPO_4 nanosheets (thickness: 3.7-4.6 nm) with exposed (010) surface facets, and the materials showed an excellent performance and delivered an initial discharge capacity of 157 $\text{mAh}\cdot\text{g}^{-1}$, 119 $\text{mAh}\cdot\text{g}^{-1}$, and 63 $\text{mAh}\cdot\text{g}^{-1}$ at 0.2 C, 5 C and 20 C, respectively.³⁰ A. Yamada et al reported a $\text{LiMn}_{0.6}\text{Fe}_{0.4}\text{PO}_4$ solid solution system and indicated that the Fe-doped LiMnPO_4 materials showed better electrochemical performances in comparison with LiMnPO_4 on account of improving the kinetics during lithiation/delithiation.³¹ H. Wang et al developed a two-step synthesis approach of $\text{LiMn}_{0.75}\text{Fe}_{0.25}\text{PO}_4$ nanorods/rmGO with a total content of 26 wt% conductive carbon, and the resulting hybrids of nanorods and graphene showed high specific capacities of 132 $\text{mAh}\cdot\text{g}^{-1}$ and 107 $\text{mAh}\cdot\text{g}^{-1}$ at high discharge rates of 20 C and 50 C.¹⁸ B. Ding et al synthesized $\text{LiMn}_{0.7}\text{Fe}_{0.3}\text{PO}_4/\text{C}$ with interspersed carbon particles by solid-state reaction, and the material showed a discharge capacity of 164 $\text{mAh}\cdot\text{g}^{-1}$ at 0.05 C and 107 $\text{mAh}\cdot\text{g}^{-1}$ at 5 C.³² However, owing to massive carbon (10 wt%) and Fe (30 mol%), the $\text{LiMn}_{0.7}\text{Fe}_{0.3}\text{PO}_4/\text{C}$ has a relatively low energy density. Based on the above results, we believe that the crystalline size, the

cationic doping of LiMnPO_4 and the rational carbon coating are the important factors in determining the reversible capacity and rate capability of LiMnPO_4 .

In this study, we report the synthesis and electrochemical performance of $\text{LiMn}_{1-x}\text{Fe}_x\text{PO}_4$ -polyacene ($x = 0$ and 0.1 , hereafter referred to as $\text{LiMn}_{1-x}\text{Fe}_x\text{PO}_4$ -PAS) prepared by the solvothermal method followed by a sintering process. The nanocrystals show a moderate crystallite size of 50–100 nm, which ameliorates the solid state diffusion of lithium within the prepared materials. The effects of polyacene on structure and performance of lithium manganese ion phosphates were extensively investigated. Introducing polyacene to integrate the nanocrystals improves the electronic conductivity of the composite significantly. Furthermore, the capacity fading of the cathode materials during cycling were studied systematically.

Experimental

$\text{LiMn}_{0.9}\text{Fe}_{0.1}\text{PO}_4$ nanomaterials were prepared by an ascorbic acid-assisted solvothermal method. All the precursors were purchased without further pre-treatment or purification. Stoichiometric amounts of $\text{LiOH}\cdot\text{H}_2\text{O}$, H_3PO_4 , $\text{MnSO}_4\cdot\text{H}_2\text{O}$ and $\text{FeSO}_4\cdot 7\text{H}_2\text{O}$ with a molar ratio of 3:1:0.9:0.1 were dissolved in 1:1 (V/V) ethanol-water solvent under stirring, and then ascorbic acid was added (molar ratio of $\text{LiMn}_{0.9}\text{Fe}_{0.1}\text{PO}_4$: ascorbic acid = 1: 2.6) into the solution. After 5 h vigorous stirring, the solution was transferred into a 100 mL Teflon-lined stainless steel autoclave, and the autoclave was put into a preset electric furnace and maintained at 200°C for 12 h. The obtained solution was filtered and washed with ethanol and distilled water several times and finally dried at 80°C in vacuum for 5 h. The $\text{LiMn}_{0.9}\text{Fe}_{0.1}\text{PO}_4$ -PAS composite was prepared as follows: $\text{LiMn}_{0.9}\text{Fe}_{0.1}\text{PO}_4$ and the desired amount of phenolic resin were mixed firstly. The mixture was ball-milled at 350 rpm for 5 h, followed by heat treatment in a tubular furnace at 300°C for 3 h, and then heated at 600°C for 5 h under a Ar/H_2 ($\text{Ar}:\text{H}_2 = 95:5$) atmosphere to obtain the final $\text{LiMn}_{0.9}\text{Fe}_{0.1}\text{PO}_4$ -PAS composite. For comparison, LiMnPO_4 -PAS composite was prepared by the same method.

The X-ray powder diffraction (XRD) patterns of the products were determined by X-ray powder diffractometer (Empyrean) equipped with $\text{Cu K}\alpha$ radiation over the 2θ range of 10° – 130° . Rietveld refinement for XRD patterns was performed using the GSAS/EXPGUI package. The manganese dissolution was evaluated by the elemental analysis using OPTIMA 5300DV ICP Optical Emission Spectrometers. Morphological profiles and Energy dispersive spectrometer (EDS) were observed by field-emission scanning electron microscope (FESEM, FEI Helios Nanolab600i). High-resolution transmission electron microscopy (HRTEM) images and selected-area electron microscopy (SAED) were taken using a FEI Tecnai G² F30 transmission electron microscope. Fourier transform infrared (FT-IR) spectra were recorded using a Thermo Scientific Nicolet iS10 (USA) over the range of 400 – 4000 cm^{-1} with spectral resolution of 4 cm^{-1} . The conductivity of the composites was measured by SB120/2 four-point probe method. X-ray photoelectron spectra (XPS, Thermo Scientific K-alpha X-ray photoelectron spectroscopy) were examined to identify the surface chemistry of the LiMnPO_4 -PAS electrode after cycling. The amount of polyacene in the composite was determined by thermogravimetric analysis (TGA) from the room temperature to 650°C at a heating rate of $10^\circ\text{C}\cdot\text{min}^{-1}$ using a Simultaneous Thermal Analysis (DSC, Netzsch STA449F3) in Ar/O_2 ($\text{Ar}: 60\text{ mL}\cdot\text{min}^{-1}$, $\text{O}_2: 20\text{ mL}\cdot\text{min}^{-1}$)

atmosphere. The BET specific surface area was calculated from nitrogen adsorption isotherms using 3H-2000PS1 surface area and pore analyzer at 77K .

Electrochemical measurement was carried out by the assembly of 2016 coin-type cell with lithium metal foil as the counter and reference electrode. The slurry was obtained by mixing 80 wt% active material, acetylene black (10 wt%), and polyvinylidene fluoride (PVDF, 10 wt%) in N-methylpyrrolidone (NMP) solvent, and then coated on the aluminum foils ($\phi=14\text{ mm}$) to form the working electrode. The mass loading in the electrode was around $2.0\text{ mg}\cdot\text{cm}^{-2}$. $1\text{ mol}\cdot\text{L}^{-1}$ LiPF_6 in a mixed solvent of ethylene carbonate (EC) and dimethyl carbonate (DMC) with 1:1 in volume ratio was used as the electrolyte. All cells were assembled in an Ar-filled glove box in which both moisture and oxygen levels were less than 1ppm. The cells were examined using a battery testing system (Neware, BST-5V3mA) at different charge/discharge rates between 2.5 and 4.6 V. The cells were charged at a CC-CV protocol, *i.e.*, first charged at a constant current of 0.1 C to 4.6 V followed by holding at 4.6 V for 30 min. Electrochemical impedance spectra (frequency range: 0.01 – 10^5 Hz) of electrodes in coin-type cells were performed with an electrochemical workstation (PARSTAT 2273).

Results and discussion

Figure 1 shows the synthesis illustration of the polyacene-coated $\text{LiMn}_{0.9}\text{Fe}_{0.1}\text{PO}_4$ materials. Pure phase $\text{LiMn}_{0.9}\text{Fe}_{0.1}\text{PO}_4$ nanoplates were prepared by an ascorbic acid-assisted solvothermal method.²² Subsequently, the mixture of pure phase $\text{LiMn}_{0.9}\text{Fe}_{0.1}\text{PO}_4$ nanoplates and phenol formaldehyde resin were ball-milled using ethanol as the dispersing agent. The as-prepared powders were annealed at 350°C for 3 h, and then heated at 600°C for 5 h under Ar/H_2 ($\text{Ar}:\text{H}_2 = 95:5$) atmosphere. The obtained PAS not only acts as a conductive coating on the surface of nanoplates in amorphous phase but also supplies a conductive matrix for the secondary $\text{LiMn}_{0.9}\text{Fe}_{0.1}\text{PO}_4$ particles. Furthermore, the phenolic resin adsorbed on the surface of $\text{LiMn}_{0.9}\text{Fe}_{0.1}\text{PO}_4$ nanoplates can suppress grain aggregation during the heat treatment. The amorphous PAS in the composite enhances the electronic conductivity by allowing electrons to tunnel quickly among the active materials. In addition, the ball milling process of the $\text{LiMn}_{0.9}\text{Fe}_{0.1}\text{PO}_4$ nanoplates and phenol formaldehyde resin also can reduce the particle size of the composite, which can shorten the solid-state diffusion path and break the barrier of the kinetic limitation for these lithium transition metal phosphates.

Figure 2 shows the X-ray diffraction patterns and Rietveld refinements of as-prepared LiMnPO_4 and $\text{LiMn}_{0.9}\text{Fe}_{0.1}\text{PO}_4$, respectively. All the diffraction patterns can be clearly indexed to an orthorhombic space group *pnma* (JCPDS No. 74-0375) and indicative of the perfect crystalline structure of LiMnPO_4 . From Figure 2a we can see that the Fe-doped sample shows a very similar diffraction profile to that of LiMnPO_4 except for the slight shift of peaks to higher diffraction angles as illustrated by (020) peak (inset of Figure 2a). In order to further explore the structural evolution affected by the Fe doping, a Rietveld refinement was conducted for the two samples (Figure 2b). The refinement results shown in Figure 2b exhibit good consistency for the experimental and the calculated XRD patterns. The reasonably small R_{wp} factor (4.91% for LiMnPO_4 and 2.91% for $\text{LiMn}_{0.9}\text{Fe}_{0.1}\text{PO}_4$) manifests that perfect crystalline olivine structure is obtained and no impurity phases can be detected. The structural parameters of the two samples

obtained from the refinement are listed in Table 1. The volume of $\text{LiMn}_{0.9}\text{Fe}_{0.1}\text{PO}_4$ decreases due to the smaller ionic radius of Fe^{2+} (9.2 Å) than that of Mn^{2+} (9.7 Å), which means the decrease of the average M-O (M = Mn and Fe) bond length after Fe substitution. The short average bond length decreases the ionicity of the Mn-O bonds in $\text{LiMn}_{0.9}\text{Fe}_{0.1}\text{PO}_4$ compared with pristine LiMnPO_4 , which can improve the electron polaron hopping between adjacent cationic centers.³² These above observations indicate that Fe partial substitution is successfully achieved to form the $\text{LiMn}_{0.9}\text{Fe}_{0.1}\text{PO}_4$ solid solution.

Figure 3a-b show that the LiMnPO_4 and $\text{LiMn}_{0.9}\text{Fe}_{0.1}\text{PO}_4$ nanoplates are 100~150 nm in length and ~30 nm in thickness. The size of the samples is 50-100 nm after ball-milling, which means that the nanoplates are small enough to provide a sufficiently large surface area (65.6 $\text{m}^2\cdot\text{g}^{-1}$ for LiMnPO_4 and 71.5 $\text{m}^2\cdot\text{g}^{-1}$ for $\text{LiMn}_{0.9}\text{Fe}_{0.1}\text{PO}_4$, Figure S1) for Li^+ transportation. Figure 3c-d present the LiMnPO_4 -PAS and $\text{LiMn}_{0.9}\text{Fe}_{0.1}\text{PO}_4$ -PAS powder consisting of the secondary particles. Interestingly, among the particles, the lamellar structure of alternating plate (Figure 3d) is formed after dehydration and dehydrocyclization during pyrolysis of the phenolic resin. The PAS contents of LiMnPO_4 -PAS and $\text{LiMn}_{0.9}\text{Fe}_{0.1}\text{PO}_4$ -PAS are 5.5 wt% and 5.6 wt%, respectively (Figure S2). From Figure S3 and S4, it can be seen that the increasing PAS content makes the agglomeration exacerbated and lowers the conductivity of the materials (Table S1). While the 3wt% PAS in the composite cannot supply the integrated conducting layer on the surface of nanoplates and the conductive network among the particles, resulting in the low conductivity for the composite. From the above mentioned, the $\text{LiMn}_{0.9}\text{Fe}_{0.1}\text{PO}_4$ -PAS composite with 5.6 wt% PAS, which exhibits the largest electrical conductivity among the samples with different content of polyacene, is expected to possess the good electrochemical performance.

The element mappings of $\text{LiMn}_{0.9}\text{Fe}_{0.1}\text{PO}_4$ -PAS (Figure 4) illustrate that all the elements, such as Mn, Fe, P, O, C and B, show a fairly uniform distribution in $\text{LiMn}_{0.9}\text{Fe}_{0.1}\text{PO}_4$ -PAS. Specifically, it can be deduced from the element distribution that the PAS is uniformly dispersed among the primary $\text{LiMn}_{0.9}\text{Fe}_{0.1}\text{PO}_4$ particles, which can be confirmed from the pleated PAS sheets coating on the surface of the particles in TEM image of $\text{LiMn}_{0.9}\text{Fe}_{0.1}\text{PO}_4$ -PAS (Figure 3e). The conductive PAS is well decentralized among $\text{LiMn}_{0.9}\text{Fe}_{0.1}\text{PO}_4$ nanoplates and on the surface of the primary nanocrystals. Furthermore, the nanoplates are coated by a layer of uniform amorphous PAS with the thickness of 2.5 nm as shown in Figure 3f. These results indicate that $\text{LiMn}_{0.9}\text{Fe}_{0.1}\text{PO}_4$ nanoplates are in intimate contact with the dispersed conductive PAS, and the primary $\text{LiMn}_{0.9}\text{Fe}_{0.1}\text{PO}_4$ particles are interconnected by a network of pleated PAS nanosheets (Figure 3b and 3c).

In order to further understand the pleated structure of conductive PAS matrix, we investigated the pyrolysis process of phenol-formaldehyde resin. Figure 5 shows the FT-IR spectra of the phenolic resin and pyrolyzates. The peaks at 3384, 2926 (2844), 1644 (1423), 1274, 1100 and 754 cm^{-1} of the phenolic resin FT-IR spectrum are in reference to the O-H

stretching vibrations, the absorption peaks of C-H₂, C=C in-plane vibrations of aromatic system, C-C stretching vibrations attached to the aromatic ring, the absorption peaks of C-B and C-H out-of-plane deformation vibrations, respectively. The presence of C-B peaks illustrates that the phenol-formaldehyde resin is modified by boron doping, which can enhance the conductivity of the pyrolyzed phenolic resin.³³ We can see that the frequencies at 3384 cm^{-1} fade quickly as the temperature increases and lower up to the minimum at 700°C. The peak at 3492 cm^{-1} is attributed to the water in the air. The strength of the absorption peaks of C-H₂ ascends at first and then descends with the increase of temperature. The C-C stretching vibrations attaching to the aromatic ring and C-H out-of-plane deformation vibrations are almost disappeared after heat treatment. At 650 °C and 700 °C, only the absorptions at about 1644 and 1423 cm^{-1} (indicated by dashed line) assign to the stretching vibration of the aromatic ring C=C are retained, which indicates that the phenolic resin possesses aromatic cyclization after the heat treatment between 600 and 700 °C. Therefore, it can be concluded that the PAS is formed at 600°C completely, which is depicted graphically in Figure S5 in the supporting Information.³⁴ These results also suggest that the intermolecular dehydration of phenolic resin happens with the consequent process of dehydrocyclization.³⁵

The initial charge/discharge curves of LiMnPO_4 -PAS and $\text{LiMn}_{0.9}\text{Fe}_{0.1}\text{PO}_4$ -PAS are shown in Figure 6a-b. Each cell was charged at a constant current rate of 0.1 C to 4.6 V, kept at 4.6 V for 30 min, and then discharged at a certain rate to 2.5 V. The $\text{LiMn}_{0.9}\text{Fe}_{0.1}\text{PO}_4$ -PAS composite material demonstrates an excellent rate capability with discharge capacities of 161, 147, 141, 115, 107, and 79 $\text{mAh}\cdot\text{g}^{-1}$ at 0.1 C, 0.5 C, 1 C, 5 C, 10 C, and 20 C, respectively. While the LiMnPO_4 -PAS sample only delivers the discharge capacities of 138, 127, 119, 95, 73, and 53 $\text{mAh}\cdot\text{g}^{-1}$ at the above mentioned rates, respectively. The discharge curves of $\text{LiMn}_{0.9}\text{Fe}_{0.1}\text{PO}_4$ -PAS demonstrate a reversible potential plateau of around 4.0 V and a slightly inclined potential plateau at 3.5 V at 0.1 C, which corresponds to the $\text{Mn}^{3+/2+}$ and $\text{Fe}^{3+/2+}$ redox reactions, respectively.^{9, 10, 18, 19, 22, 32, 36} For LiMnPO_4 -PAS, there is only one potential plateau at around 4.0 V for the $\text{Mn}^{3+/2+}$ reaction.

The cycle performance of the LiMnPO_4 -PAS and $\text{LiMn}_{0.9}\text{Fe}_{0.1}\text{PO}_4$ -PAS composites at room temperature is shown in Figure 6c. It can be seen that the reversible discharge capacity after 100 cycles of LiMnPO_4 -PAS decreases by about 26% and 28% at 10 C and 20 C, respectively. However, $\text{LiMn}_{0.9}\text{Fe}_{0.1}\text{PO}_4$ -PAS nanoplates still retain the reversible discharge capacities of 96 and 71 $\text{mAh}\cdot\text{g}^{-1}$ at the 100th cycle at 10 C and 20 C, which corresponds to 89.7% and 89.8% of their initial discharge capacities, respectively. The rate performance of the samples is shown in Figure 6d. The discharge capacities of $\text{LiMn}_{0.9}\text{Fe}_{0.1}\text{PO}_4$ -PAS composite electrode are 138, 104 and 76 $\text{mAh}\cdot\text{g}^{-1}$ at discharge rates of 1 C, 10 C and 20 C, respectively. After 55 cycles, the $\text{LiMn}_{0.9}\text{Fe}_{0.1}\text{PO}_4$ -PAS delivers a reversible discharge capacity of 144 $\text{mAh}\cdot\text{g}^{-1}$ which is higher than 125 $\text{mAh}\cdot\text{g}^{-1}$ for LiMnPO_4 -PAS electrode when the discharge rate is reduced back to 0.1 C. These results indicate

that the $\text{LiMn}_{0.9}\text{Fe}_{0.1}\text{PO}_4$ -PAS composite has an excellent rate performance due to the iron doping and the conductive PAS matrix for LiMnPO_4 cathode material. Moreover, compared with our previous work on $\text{LiMn}_{0.9}\text{Fe}_{0.1}\text{PO}_4$ coated by 10 wt% of carbon,²² the $\text{LiMn}_{0.9}\text{Fe}_{0.1}\text{PO}_4$ with only 5.6 wt% PAS exhibits the superior electrochemical performance. The excellent electrochemical performance of $\text{LiMn}_{0.9}\text{Fe}_{0.1}\text{PO}_4$ -PAS composite is mainly attributed to (i) the well-distributed conductive PAS matrix supplying the electrically conductive paths for electrons; (ii) a smaller nanometer-scale primary $\text{LiMn}_{0.9}\text{Fe}_{0.1}\text{PO}_4$ particles shortening the diffusion length for the Li^+ ions,¹⁶ and improving the state-of-charge metastable stability;³⁷ (iii) the improvement in the (electronic and ionic) transport properties of the nanocrystals related to the Fe substitution.^{18, 19, 37}

The Capacity Degradation Analysis of Olivine-type phosphate cathodes

From Figure 6, it can be seen that the $\text{LiMn}_{1-x}\text{Fe}_x\text{PO}_4$ -PAS ($x=0$ and 0.1) composites still show a slight capacity decay during cycling. We prepared the LiMnPO_4 -PAS and $\text{LiMn}_{0.9}\text{Fe}_{0.1}\text{PO}_4$ -PAS composite to further comprehend the capacity evolution in term of the manganese dissolution firstly. For comparison, the LiMnPO_4 -C was also prepared by the same method using glucose as carbon source. All the materials were prepared with similar morphology, particle size and carbon content. The Mn dissolution analysis was performed on a fully charged electrode using the ICP technique, and Mn dissolution rate in the electrolyte at room temperature was investigated by aging the electrode after soaking the charged (4.6 V) in the electrolyte at room temperature for 30 days. The results shown in Table 2 indicate that Mn dissolution is retarded by the PAS coating and the Fe-doping. The Mn dissolution concentration in LiMnPO_4 -PAS was 4.613 ppm which is much lower than that in LiMnPO_4 -C (9.352 ppm). Such a tendency is suggestive of the fact that the PAS on the surface of the nanocrystalline and among the particles can also avoid the electrode contact with electrolyte directly, which protects them against the HF attack during cycling and thus reduces the Mn dissolution into the electrolyte.³⁸ Among the three electrodes, the $\text{LiMn}_{0.9}\text{Fe}_{0.1}\text{PO}_4$ -PAS electrode has the lowest amount of Mn dissolution in comparison with the LiMnPO_4 -C and LiMnPO_4 -PAS, which indicates that the introduced Fe in the solid solution can improve the transport (electronic and ionic) properties of the nanocrystals. Moreover, the Fe-doping can suppress the Jahn-Teller distortion of active Mn^{3+} ions which gives a big structural misfit at the phase boundary between lithiated and delithiated phases.^{23, 37}

In general, the high charging potential will accelerate the decomposition of electrolyte. In order to further understand this phenomenon about the two electrodes, the EDS of the two electrodes before and after 50 cycles at 0.5 C were measured (Figure 7a-d). From Figure 7e-f we can see that no obvious variations are observed for both electrodes on the content of C, O, P and Mn elements after cycling. However, the contents of F

element on the surface of LiMnPO_4 -PAS and $\text{LiMn}_{0.9}\text{Fe}_{0.1}\text{PO}_4$ -PAS electrodes increase dramatically from 5.86% and 6.17% to 10.66% and 9.55% respectively, which means that some side reactions related to the electrolyte have occurred during the charge-discharge process.

The $\text{LiMn}_{1-x}\text{Fe}_x\text{PO}_4$ -PAS ($x=0$ and 0.1) electrodes before and after cycling were examined by performing XPS analysis to understand the content change of F element (Figure 8). Before cycling the F 1s peaks in both compounds (Figure 8c) only show a binding energy of 686.5 eV, which is in good agreement with the reported result for PVDF^{39, 40}. However, this F 1s peak can be deconvoluted into two different peaks centred at 686.5 and 684.5 eV after cycling, corresponding to PVDF and LiF ⁴¹, respectively. The P 2p peak (Figure 8d) on the two electrodes shows a binding energy of 133.2 eV before cycling, which is the characteristic of the tetrahedral PO_4 group^{42, 43}. In addition, P-F peak (136.4 eV)^{40, 41} corresponding to PF_5 which was formed due to the LiPF_6 decomposition during charge-discharge process⁴¹, is observed on both electrodes after cycling. No significant changes are observed on the two samples in Mn 2p core spectrum (before cycling Figure 8e and after cycling Figure 8h) which splits into two peaks due to spin-orbit coupling ($\text{Mn}2p_{1/2}$: 653.0 eV and $\text{Mn}2p_{3/2}$: 641.4 eV with a “shake-up” satellite at 646.4 eV)^{44, 45}, and so is the same for the Fe 2p core spectrum ($\text{Fe}2p_{1/2}$: 724.7 eV and $\text{Fe}2p_{3/2}$: 710.8 eV)⁴³ in the $\text{LiMn}_{0.9}\text{Fe}_{0.1}\text{PO}_4$ -PAS composite. From the above mentioned, it can be concluded that the capacity degradation of olivine-type lithium manganese/iron phosphate materials is related to the side reactions of the electrolyte decomposition during the charge-discharge process⁴¹.

As we all know, the structure of material has an important effect on the properties. In order to further explore the structural changes during delithiation/lithiation, a Rietveld refinement was performed on $\text{LiMn}_{1-x}\text{Fe}_x\text{PO}_4$ -PAS ($x=0$ and 0.1) electrodes before and after cycling (Figure 9). We can see that after cycling both samples give the very similar diffraction profiles. All the diffraction patterns can be clearly indexed to an orthorhombic space group *pnma*, and no impurities are detected for the two electrodes. The structural parameters of the two samples obtained from the refinement are listed in Table 3. The reasonably small R_{wp} factors manifest that perfect crystalline olivine structure is maintained during the charge-discharge process and no other impurities are formed. The antisite defects Mn_{Li} of $\text{LiMn}_{0.9}\text{Fe}_{0.1}\text{PO}_4$ -PAS electrode just have a slight increase by 4% after cycling from 6.7% to 7.9% in comparison with the LiMnPO_4 -PAS electrode. The relatively small increase of antisite defects for $\text{LiMn}_{0.9}\text{Fe}_{0.1}\text{PO}_4$ -PAS manifests that the Fe^{2+} in the crystal structure can stabilize the crystals during charge-discharge and enhance electrochemical performance of this kind of cathode material.⁴⁶

In order to further confirm the increasing antisite defects, the $\text{LiMn}_{1-x}\text{Fe}_x\text{PO}_4$ -PAS ($x=0$ and 0.1) electrodes were characterized by FT-IR (Figure 10). In olivine-type materials, the PO_4 tetrahedron will be affected by the surrounding MnO_6 and LiO_6 octahedrons. Hence, the Mn_{Li} antisite defects may induce the change of the P-O bonds in the PO_4 tetrahedrons,

which reflects a shift of the vibration frequencies of P-O bonds on the FT-IR curves. The red shift of P-O symmetric stretching vibration peak means an increase in the antisite defect concentration.⁴⁷ From Figure 10, we can see that the peaks at approximate 970 and 1041 cm^{-1} originate from the P-O symmetric and asymmetric stretching vibrations of the olivine phosphate groups, respectively. The pink asterisks correspond to the peaks of PVDF. The P-O symmetric stretching vibration peak of the LiMnPO_4 -PAS shifts to 975.8 cm^{-1} from 970.8 cm^{-1} after cycling, which indicates that the defect concentration of Mn_{Li} in the composite increases. However, the P-O peak of the $\text{LiMn}_{0.9}\text{Fe}_{0.1}\text{PO}_4$ -PAS electrode only shifts by 0.8 cm^{-1} relatively. These results agree well with the XRD patterns (Figure 9). Hence, the raised Mn_{Li} antisite defect in the crystal structure is a significant cause of the performance degradation during the charge-discharge process.

In order to observe the antisite defects directly, the LiMnPO_4 -PAS composite before and after cycling was characterized by TEM, and the images are shown in Figure 11. The selected area electron diffraction patterns of LiMnPO_4 -PAS after cycling (Figure 11a-b) are similar to that of the materials before cycling, which indicates that the single-crystal structure of the composites is maintained. The HRTEM images of LiMnPO_4 -PAS show the interplanar spacing of 3.9 Å (before cycling, Figure 11c, d) and 2.8 Å (after cycling, Figure 11f, g) which can be referred to the crystallographic directions of (210) and (301), respectively. In addition, HRTEM images further verify the highly ordered single crystalline structure for the two samples. However, from the FFT images, we can see that additional diffraction spots (indicated by yellow circle) corresponding to the Mn_{Li} antisite defects are detected for cycled material (Figure 11h), indicating the lower degree of crystallinity compared with the LiMnPO_4 -PAS without cycling. Schematic illustration of the highly ordered single crystalline structure of LiMnPO_4 before cycling and the Mn_{Li} antisite defects in the structure after cycling are shown in Figure 11i-j.

The resistances of $\text{LiMn}_{1-x}\text{Fe}_x\text{PO}_4$ -PAS ($x=0$ and 0.1) electrodes before and after cycling were measured, and the resulting electrochemical impedance spectra (EIS) are presented as Nyquist plots in Figure 12. As can be seen from Figure 12a, each EIS profile exhibits a semicircle in the high frequency region and an inclined line in the low frequency region. An intercept at the Z' axis in high frequency represents the ohmic resistance of the aqueous electrolyte (R_e). The semicircle in the high frequency range corresponds to the charge transfer process, and the diameter of the semicircle on the Z' axis corresponds to the charge transfer resistance (R_{ct}). The R_{ct} of both electrodes increases after cycling, which is correlated with by-products (Figure 8) on the electrode surface and the increasing Mn_{Li} antisite defects in the structure. The straight line in the low frequency is attributed to the Warburg impedance (Z_w), which denotes the Li^+ diffusion resistance through the active cathode material. Therefore, the Li^+ diffusion coefficient (D) of the cathode material can be calculated according to the following equations:

$$D = \frac{R^2 T^2}{2n^2 A^2 F^4 C^2 \sigma^2} \quad (1)$$

$$Z'' = \sigma \omega^{-1/2} \quad (2)$$

Where, R is the gas constant, T is the absolute temperature, A is the surface of the cathode (its value calculated by BET method, Figure S1), n is the number of electrons involved in the redox process ($n = 1$ for $\text{Mn}^{2+}/\text{Mn}^{3+}$ redox pair), F is the Faraday constant, C is the shuttle concentration, and σ is the Warburg factor which is related to Z'' . Figure 12b illustrates the linear relationship between Z'' and the inverse square root of angular frequency. According to the slope of the line and eqs (1) and (2), we can calculate the D of the two electrodes before and after cycling as listed in Table 4. Obviously, the Li^+ diffusion coefficients for both electrodes increase after cycling, which is mainly due to the raised concentration of antisite defects in the crystal structure.

Conclusions

High-performance nanostructured $\text{LiMn}_{0.9}\text{Fe}_{0.1}\text{PO}_4$ powders were prepared by a solvothermal method. Simultaneously, the $\text{LiMn}_{0.9}\text{Fe}_{0.1}\text{PO}_4$ nanocrystalline was successfully coated with the uniform conductive PAS layer by pyrolysis of the phenolic resin, and the secondary particles consisting of primary $\text{LiMn}_{0.9}\text{Fe}_{0.1}\text{PO}_4$ nanocrystals with PAS matrix formed. The $\text{LiMn}_{0.9}\text{Fe}_{0.1}\text{PO}_4$ -PAS composite with high conductivity delivers a discharge capacity of 161, 147, 141, 115, 107, and 79 $\text{mAh}\cdot\text{g}^{-1}$ at 0.1 C, 0.5 C, 1 C, 5 C, 10 C, and 20 C, respectively, and it can retain 90% of the initial reversible capacity even after 100 cycles at a rate of 20 C. The improved electrochemical performance is ascribed to the homogeneous conductive PAS coating and the well dispersed PAS network, which protects the $\text{LiMn}_{0.9}\text{Fe}_{0.1}\text{PO}_4$ -PAS against HF attack, and leads to an obvious reduction of Mn dissolution and a greatly enhanced electronic conductivity. The Mn_{Li} antisite defects, Mn dissolution and electrolyte decomposition are considered as the determining factors for capacity fading during charge-discharge process of the lithium manganese phosphate class cathode materials.

Acknowledgements

This work was partially supported by The Natural Science Foundation of China (no. 50902038), National High Technology Research and Development Program (863 Program) of China (no. 2012AA110203) and Heilong Jiang Postdoctoral Funds for Scientific Research Initiation (no. LBH-Q12084).

Notes and references

a School of Chemical Engineering and Technology, Harbin Institute of Technology, No.92 West-Da Zhi Street, Harbin 150001, China.

E-mail: zuopj@hit.edu.cn, zuopjhit@gmail.com (P. Zuo).

Tel./fax: +86-451-86403216.

† Footnotes should appear here. These might include comments relevant to but not central to the matter under discussion, limited experimental and spectral data, and crystallographic data.

Electronic Supplementary Information (ESI) available: The specific surface and pore size analysis of $\text{LiMn}_{0.9}\text{Fe}_{0.1}\text{PO}_4$ with 5.6 wt% of PAS and LiMnPO_4 -PAS; The SEM images of the other four composites; Conductivity of $\text{LiMn}_{0.9}\text{Fe}_{0.1}\text{PO}_4$ -PAS powders with different amount of PAS; The formation process of PAS; TG curves of LiMnPO_4 -PAS and $\text{LiMn}_{0.9}\text{Fe}_{0.1}\text{PO}_4$ -PAS samples; Initial charge/discharge curves of $\text{LiMn}_{0.9}\text{Fe}_{0.1}\text{PO}_4$ -PAS with different amount of PAS; Cycling stability of Li/ $\text{LiMn}_{0.9}\text{Fe}_{0.1}\text{PO}_4$ -PAS cells with different amounts of PAS at 5 C rate; Nyquist plots of Li/ $\text{LiMn}_{0.9}\text{Fe}_{0.1}\text{PO}_4$ -PAS cells with different amounts of PAS.[details of any supplementary information available should be included here]. See DOI: 10.1039/b000000x/

1. Y. K. Sun, S. T. Myung, B. C. Park, J. Prakash, I. Belharouak and K. Amine, *Nat. mater.*, 2009, 8, 320-324.
2. Y. K. Sun, S. T. Myung, M. H. Kim, J. Prakash and K. Amine, *J. Am. Chem. Soc.*, 2005, 127, 13411-13418.
3. A. K. Padhi, K. S. Nanjundaswamy and J. B. Goodenough, *J. Electrochem. Soc.*, 1997, 144, 1188-1194.
4. S. Y. Chung, J. T. Bloking and Y. M. Chiang, *Nat. mater.*, 2002, 1, 123-128.
5. G. Rousse, J. R. Carvajal, S. Patoux and C. Masquelier, *Chem. Mater.*, 2003, 15, 4082-4090.
6. M. Yonemura, A. Yamada, Y. Takei, N. Sonoyama and R. Kanno, *J. Electrochem. Soc.*, 2004, 151, A1352-A1356.
7. C. Delacourt, L. Laffont, R. Bouchet, C. Wurm, J. B. Leriche, M. Morcrette, J. M. Tarascon and C. Masquelier, *J. Electrochem. Soc.*, 2005, 152, A913-A921.
8. D. Morgan, A. Van der Ven and G. Ceder, *Electrochem. Solid-State Lett.*, 2004, 7, A30-A32.
9. C. M. Burba and R. Frech, *J. Power Sources*, 2007, 172, 870-876.
10. A. Yamada, Y. Kudo and K. Y. Liu, *J. Electrochem. Soc.*, 2001, 148, A1153-A1158.
11. L. F. J. Piper, N. F. Quackenbush, S. Sallis, D. O. Scanlon, G. W. Watson, K. W. Nam, X. Q. Yang, K. E. Smith, F. Omenya, N. A. Chernova and M. S. Whittingham, *J. Phys. Chem. C*, 2013, 117, 10383-10396.
12. G. B. Zhong, Y. Y. Wang, Z. C. Zhang and C. H. Chen, *Electrochim. Acta*, 2011, 56, 6554-6561.
13. C. Delacourt, P. Poizot, M. Morcrette, J. M. Tarascon and C. Masquelier, *Chem. Mater.*, 2004, 16, 93-99.
14. A. Manthiram, M. A. Vadivel, A. Sarkar and T. Muraliganth, *Energy Environ. Sci.*, 2008, 1, 621-638.
15. D. Choi, D. Wang, I. T. Bae, J. Xiao, Z. Nie, W. Wang, V. V. Viswanathan, Y. J. Lee, J. G. Zhang, G. L. Graff, Z. Yang and J. Liu, *Nano Lett.*, 2010, 10, 2799-2805.
16. R. Malik, D. Burch, M. Bazant and G. Ceder, *Nano Lett.*, 2010, 10, 4123-4127.
17. S. M. Oh, S. W. Oh, C. S. Yoon, B. Scrosati, K. Amine and Y. K. Sun, *Adv. Funct. Mater.*, 2010, 20, 3260-3265.
18. H. Wang, Y. Yang, Y. Liang, L. F. Cui, H. S. Casalongue, Y. Li, G. Hong, Y. Cui and H. Dai, *Angew. Chem.*, 2011, 123, 7502-7506.
19. S. K. Martha, J. Grinblat, O. Haik, E. Zinigrad, T. Drezen, J. H. Miners, I. Exnar, A. Kay, B. Markovsky and D. Aurbach, *Angew. Chem. Int. Ed.*, 2009, 48, 8559-8563.
20. L. Li, J. Liu, L. Chen, H. Xu, J. Yang and Y. Qian, *RSC Adv.*, 2013, 3, 6847-6852.
21. Z. Qin, X. Zhou, Y. Xia, C. Tang and Z. Liu, *J. Mater. Chem.*, 2012, 22, 21144-21153.
22. P. Zuo, G. Cheng, L. Wang, Y. Ma, C. Du, X. Cheng, Z. Wang and G. Yin, *J. Power Sources*, 2013, 243, 872-879.
23. Y. Dong, H. Xie, J. Song, M. Xu, Y. Zhao and J. B. Goodenough, *J. Electrochem. Soc.*, 2012, 159, A995-A998.
24. O. Clemens, M. Bauer, R. Haberkorn, M. Springborg and H. P. Beck, *Chem. Mater.*, 2012, 24, 4717-4724.
25. C. Hu, H. Yi, H. Fang, B. Yang, Y. Yao, W. Ma and Y. Dai, *Electrochem. Commun.*, 2010, 12, 1784-1787.
26. J. Ni, Y. Han, L. Gao and L. Lu, *Electrochem. Commun.*, 2013, 31, 84-87.
27. J. Ni and L. Gao, *J. Power Sources*, 2011, 196, 6498-6501.
28. R. Malik, F. Zhou and G. Ceder, *Phys. Rev. B*, 2009, 79, 214201-214206.
29. D. Rangappa, K. Sone, Y. Zhou, T. Kudo and I. Honma, *J. Mater. Chem.*, 2011, 21, 15813-15818.
30. X. Rui, X. Zhao, Z. Lu, H. Tan, D. Sim, H. H. Hng, R. Yazami, T. M. Lim and Q. Yan, *ACS Nano*, 2013, 7, 5637-5646.
31. A. Yamada, Y. Kudo and K.-Y. Liu, *J. Electrochem. Soc.*, 2001, 148, A747-A754.
32. B. Ding, P. Xiao, G. Ji, Y. Ma, L. Lu and J. Y. Lee, *ACS appl. mater. interfaces*, 2013, 5, 12120-12126.
33. H. Q. Xiang, S. B. Fang and Y. Y. Jiang, *Solid State Ionics*, 2002, 148, 35-43.
34. H. M. Xie, R. S. Wang, J. R. Ying, L. Y. Zhang, A. F. Jalbout, H. Y. Yu, G. L. Yang, X. M. Pan and Z. M. Su, *Adv. Mater.*, 2006, 18, 2609-2613.
35. K. A. Trick and T. E. Saliba, *Carbon*, 1995, 33, 1509-1515.
36. S. M. Oh, S. T. Myung, Y. S. Choi, K. H. Oh and Y. K. Sun, *J. Mater. Chem.*, 2011, 21, 19368-19374.
37. D. B. Ravnsbaek, K. Xiang, W. Xing, O. J. Borkiewicz, K. M. Wiaderek, P. Gionet, K. W. Chapman, P. J. Chupas and Y. M. Chiang, *Nano Lett.*, 2014, 14, 1484-1491.
38. Z. H. Chen, Y. Qin, K. Amine and Y. K. Sun, *J. Mater. Chem.*, 2010, 20, 7606-7612.
39. Yi-Chun Lu, Azzam N. Mansour, Naoaki Yabuuchi and Y. Shao-Horn, *Chem. Mater.*, 21, 4408-4424.
40. D. Choi, J. Xiao, Y. J. Choi, J. S. Hardy, M. Vijayakumar, M. S. Bhuvaneshwari, J. Liu, W. Xu, W. Wang, Z. Yang, G. L. Graff and J.-G. Zhang, *Energy Environ. Sci.*, 2011, 4, 4560-4566.
41. M. Hellqvist Kjell, S. Malmgren, K. Ciosek, M. Behm, K. Edström and G. Lindbergh, *J. Power Sources*, 2013, 243, 290-298.
42. S. K. Martha, J. Grinblat, O. Haik, E. Zinigrad, T. Drezen, J. H. Miners, I. Exnar, A. Kay, B. Markovsky and D. Aurbach, *Angew. Chem. Int. Ed.*, 2009, 48, 8559-8563.
43. K. Saravanan, M. V. Reddy, P. Balaya, H. Gong, B. V. R. Chowdari and J. J. Vittal, *J. Mater. Chem.*, 2009, 19, 605-610.
44. S. Kowalczyk, L. Ley, F. McFeely and D. Shirley, *Phys. Rev. B*, 1975, 11, 1721-1727.
45. S.-L. Yang, R.-G. Ma, M.-J. Hu, L.-J. Xi, Z.-G. Lu and C. Y. Chung, *J. Mater. Chem.*, 2012, 22, 25402-25408.
46. R. Malik, D. Burch, M. Bazant and G. Ceder, *Nano Lett.*, 2010, 10, 4123-4127.
47. Y. Zhang, N. Zhang, Z. R. Tang and Y. J. Xu, *Phys. Chem. Chem. Phys.*, 2012, 14, 9167-9175.

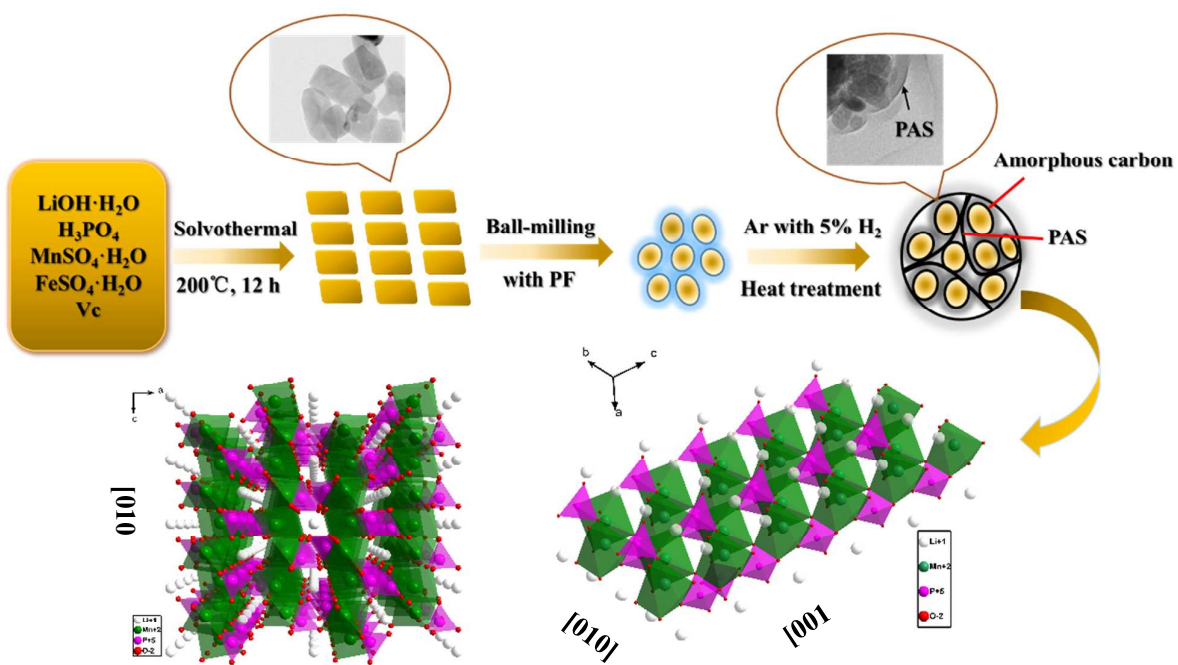
Figure 1. Schematic illustration of the preparation of $\text{LiMn}_{0.9}\text{Fe}_{0.1}\text{PO}_4$ -PAS.

Figure 2. (a) XRD patterns of LiMnPO_4 and $\text{LiMn}_{0.9}\text{Fe}_{0.1}\text{PO}_4$ samples; (b) Rietveld refinement of the XRD patterns of LiMnPO_4 and $\text{LiMn}_{0.9}\text{Fe}_{0.1}\text{PO}_4$.

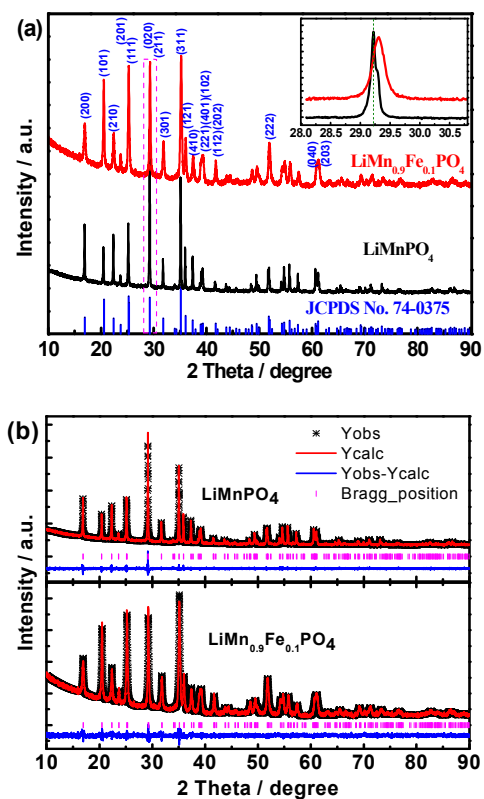


Figure 3. SEM images of (a) LiMnPO_4 ; (b) $\text{LiMn}_{0.9}\text{Fe}_{0.1}\text{PO}_4$; (c) LiMnPO_4 -PAS; (d) $\text{LiMn}_{0.9}\text{Fe}_{0.1}\text{PO}_4$ -PAS. (e) TEM image of $\text{LiMn}_{0.9}\text{Fe}_{0.1}\text{PO}_4$ -PAS; (f) HRTEM image of $\text{LiMn}_{0.9}\text{Fe}_{0.1}\text{PO}_4$ -PAS.

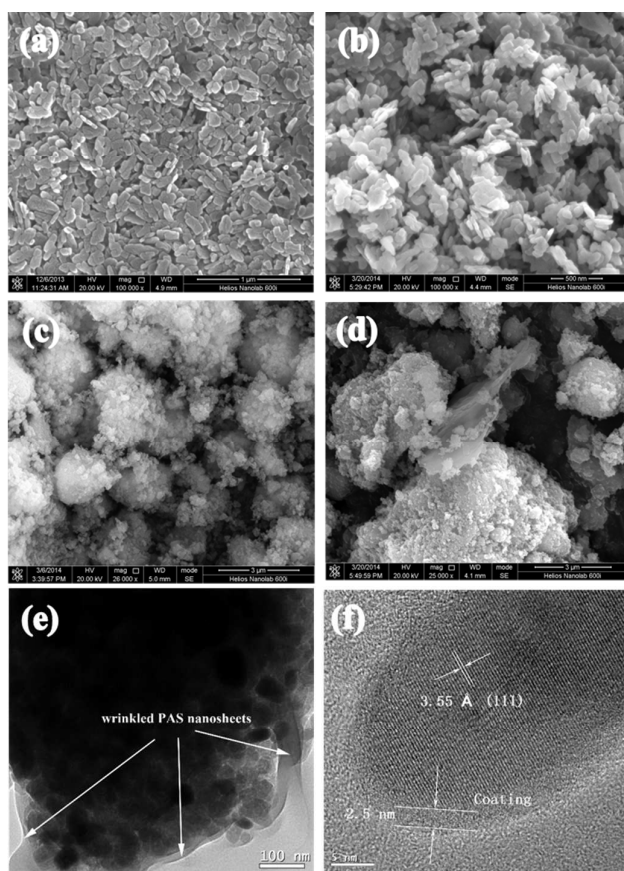


Figure 4. Element mappings of $\text{LiMn}_{0.9}\text{Fe}_{0.1}\text{PO}_4\text{-PAS}$.

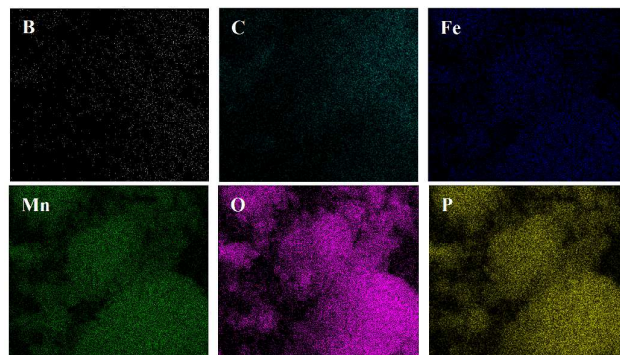


Figure 5. FT-IR absorption spectra of PAS at different temperatures and phenolic resin.

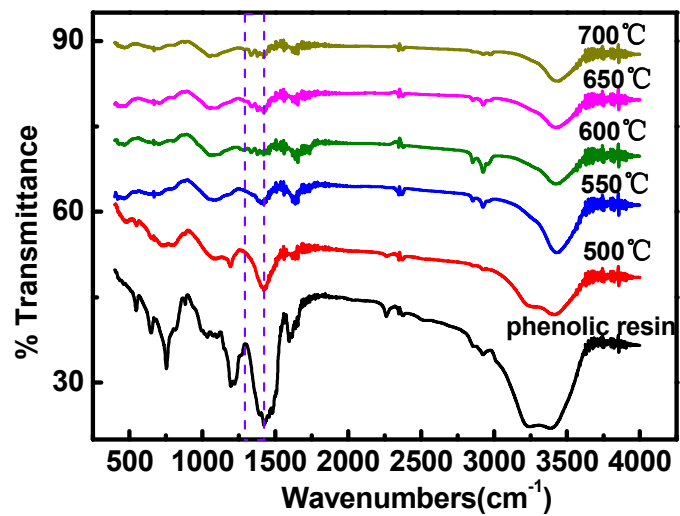


Figure 6. Initial charge/discharge curves of (a) $\text{LiMnPO}_4\text{-PAS}$ and (b) $\text{LiMn}_{0.9}\text{Fe}_{0.1}\text{PO}_4\text{-PAS}$; (c) Cycling performance of $\text{LiMnPO}_4\text{-PAS}$ and $\text{LiMn}_{0.9}\text{Fe}_{0.1}\text{PO}_4\text{-PAS}$ at 10 C and 20 C; (d) Rate performance of $\text{LiMnPO}_4\text{-PAS}$ and $\text{LiMn}_{0.9}\text{Fe}_{0.1}\text{PO}_4\text{-PAS}$.

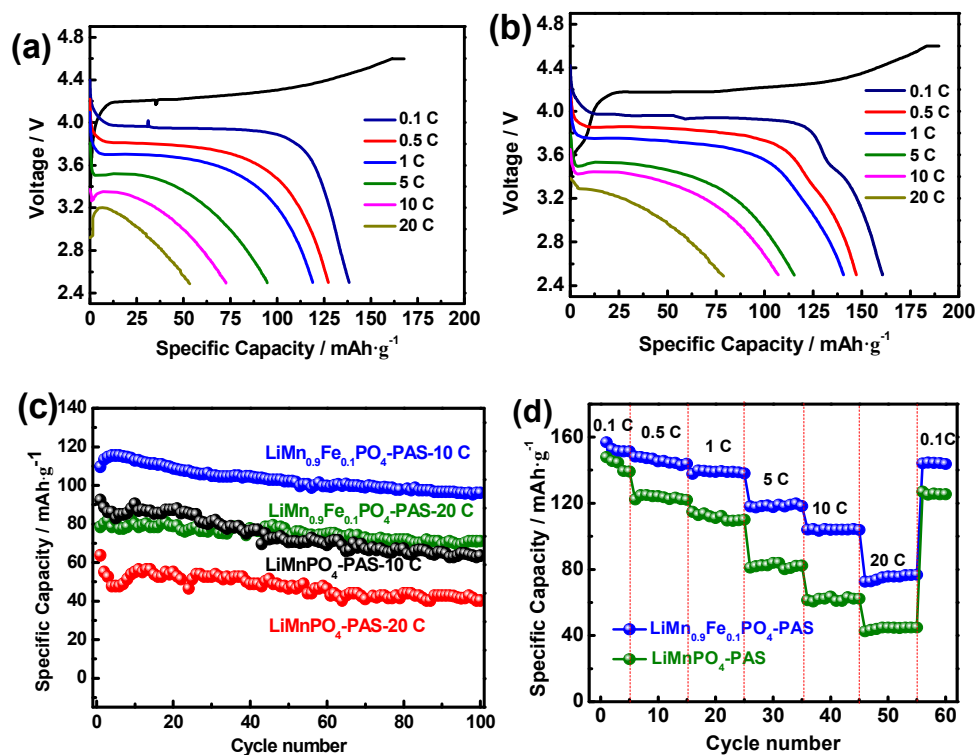


Figure 7. The EDS images of the electrode: LiMnPO_4 -PAS electrode (a) before cycling and (b) after cycling; $\text{LiMn}_{0.9}\text{Fe}_{0.1}\text{PO}_4$ -PAS electrode (c) before cycling; (d) after cycling. The element content of (e) LiMnPO_4 -PAS electrode; (f) $\text{LiMn}_{0.9}\text{Fe}_{0.1}\text{PO}_4$ -PAS electrode.

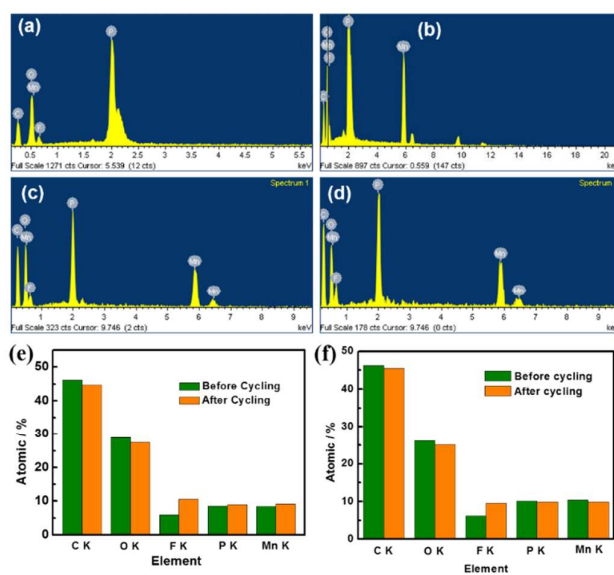


Figure 8. XPS spectra of LiMnPO_4 -PAS electrode (a-c) before cycling; (d-f) after cycling and $\text{LiMn}_{0.9}\text{Fe}_{0.1}\text{PO}_4$ -PAS electrode (g-i) before cycling; (k-n) after cycling.

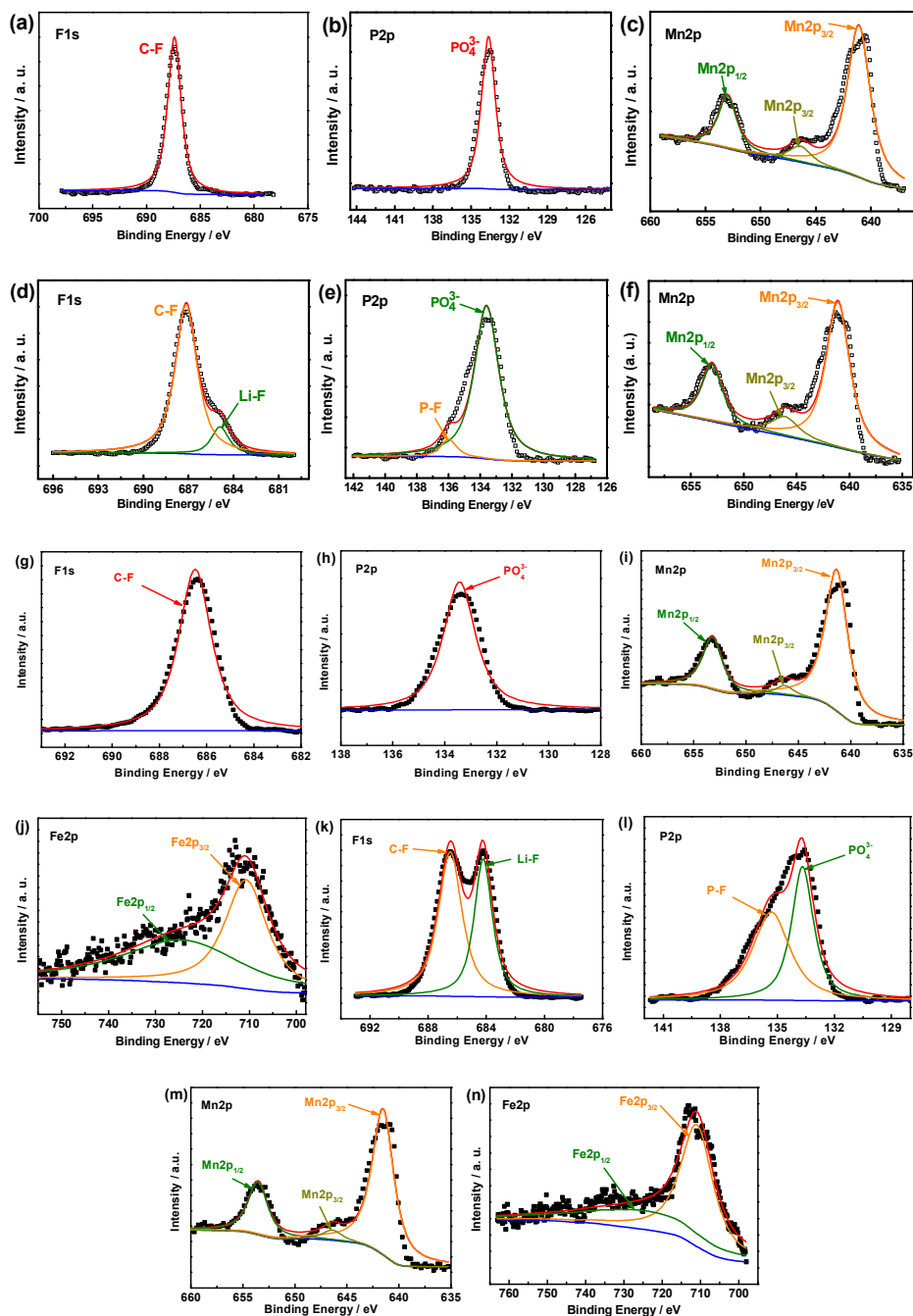


Figure 9. The XRD patterns of LiMnPO_4 -PAS electrode (a) before cycling; (b) after cycling and $\text{LiMn}_{0.9}\text{Fe}_{0.1}\text{PO}_4$ -PAS electrode (c) before cycling; (d) after cycling.

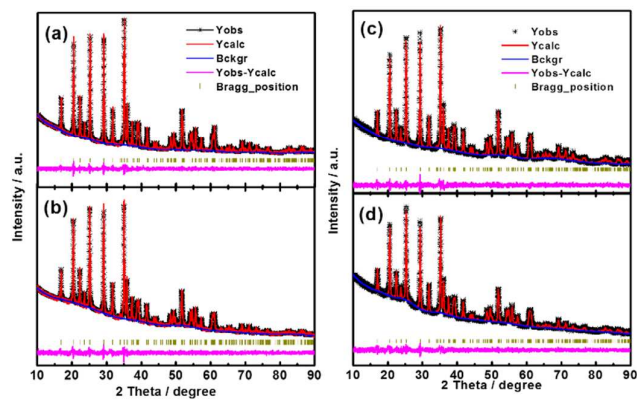


Figure 10. (a) The FT-IR curves of LiMnPO_4 -PAS and $\text{LiMn}_{0.9}\text{Fe}_{0.1}\text{PO}_4$ -PAS; (b) the magnification of the rectangle area.

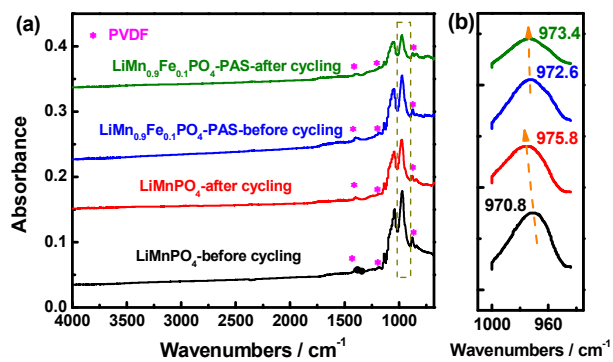


Figure 11. SAED images of LiMnPO_4 -PAS electrode: (a) before cycling and (b) after cycling. HRTEM and FFT images of LiMnPO_4 -PAS electrode: (c-e) before cycling and (f-h) after cycling. Crystal structure of LiMnPO_4 : (i) before cycling and (j) after cycling.

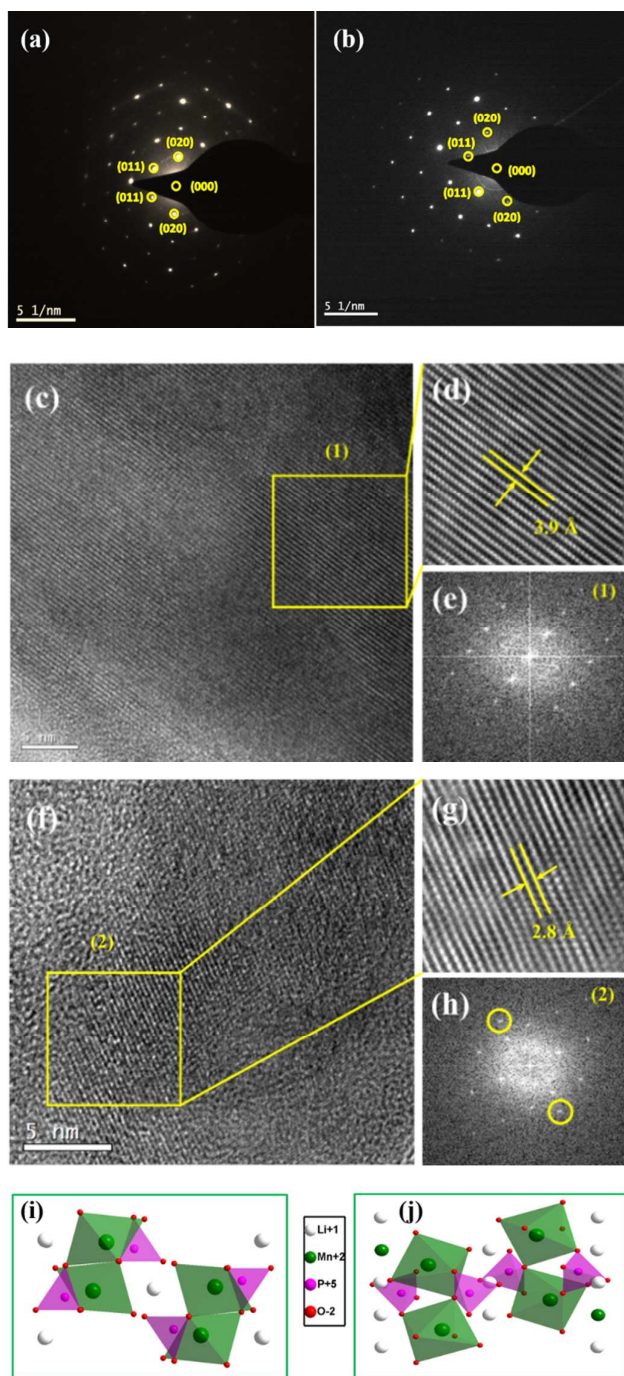


Figure 12. (a) Nyquist plots (Z' vs. $-Z''$) of the samples; (b) the relationship plot of Z' vs. $\omega^{-1/2}$ at low-frequency region.

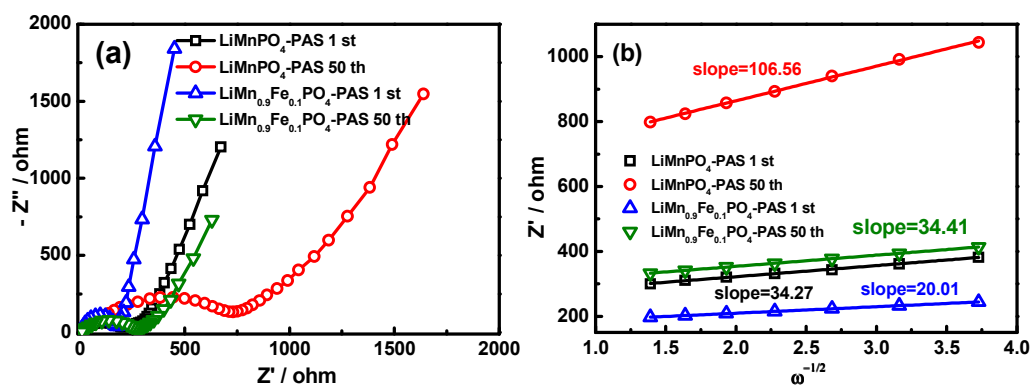


Table 1. Structure parameters of LiMnPO₄ and LiMn_{0.9}Fe_{0.1}PO₄ samples.

Samples	<i>a</i> /Å	<i>b</i> /Å	<i>c</i> /Å	<i>V</i> /Å ³	<i>R</i> _w <i>p</i> /%	<i>R</i> _p /%	χ ²
LiMnPO ₄	10.471	6.109	4.766	304.87	4.91	3.20	1.504
LiMn _{0.9} Fe _{0.1} PO ₄	10.449	6.095	4.749	302.44	2.91	2.11	1.484

Table 2. Mn dissolution in electrolyte of LiMnPO₄-C, LiMnPO₄-PAS and LiMn_{0.9}Fe_{0.1}PO₄-PAS electrodes.

	LiMnPO ₄ -C	LiMnPO ₄ -PAS	LiMn _{0.9} Fe _{0.1} PO ₄ -PAS
Mn dissolution (ppm)	9.352	4.613	1.147

Table 3. The lattice parameters of the samples.

Samples		<i>a</i> /Å	<i>b</i> /Å	<i>c</i> /Å	<i>V</i> /Å ³	<i>R</i> _w <i>p</i> /%	<i>R</i> _p /%	χ ²	Mn _{Li} /%
LiMnPO ₄ -PAS	Before cycling	10.465	6.113	4.751	303.93	2.12	1.56	1.454	5.1
	After cycling	10.458	6.109	4.760	304.10	2.46	1.91	1.337	9.1
LiMn _{0.9} Fe _{0.1} PO ₄ -PAS	Before cycling	10.439	6.100	4.744	302.08	2.48	1.77	1.394	6.7
	After cycling	10.438	6.098	4.747	302.15	2.01	1.63	1.265	7.9

Table 4. The Li⁺ diffusion coefficients of the electrodes.

Samples	D/cm ² ·S ⁻¹	
LiMnPO ₄ -PAS	Before cycling	5.96×10 ⁻¹⁴
	After cycling	4.21×10 ⁻¹⁵
LiMn _{0.9} Fe _{0.1} PO ₄ -PAS	Before cycling	1.75×10 ⁻¹³
	After cycling	5.91×10 ⁻¹⁴